Nanoscale

High-throughput Sequential Excitation for Nanoscale Mapping of Electrochemical Strain in Granular Ceria

Journal:	*Nanoscale*
Manuscript ID	NR-ART-08-2019-007438.R1
Article Type:	Paper
Date Submitted by the Author:	11-Nov-2019

Complete List of Authors:	Huang, Boyuan; University of Washington Seattle Campus Esfahani, Ehsan; University of Washington Seattle Campus Yu, Junxi; Shenzhen Institutes of Advanced Technology Chinese Academy of Sciences Gerwe, Brian; University of Washington Seattle Campus Adler, Stuart; University of Washington Seattle Campus Li, Jiangyu; Univ. of Washington,

High-throughput Sequential Excitation for Nanoscale Mapping of Electrochemical Strain in Granular Ceria

Boyuan Huang,[1,2] Ehsan Nasr Esfahani,[1] Junxi Yu,[2,3] Brian S Gerwe,[4] Stuart B. Adler,[4] and Jiangyu Li[1,2,*]

1. Department of Mechanical Engineering, University of Washington, Seattle, WA 98195, USA
2. Shenzhen Key Laboratory of Nanobiomechanics, Shenzhen Institutes of Advanced Technology, Chinese Academy of Sciences, Shenzhen, Guangdong, 518055, China.
3. Key Laboratory of Low Dimensional Materials and Application Technology of Ministry of Education, and School of Materials Science and Engineering, Xiangtan University, Xiangtan, Hunan, 411105, China
4. Department of Chemical Engineering, University of Washington, Seattle, WA 98195, USA.

Abstract

Dynamic strain based atomic force microscopy (AFM) modes often fail at the interfaces where the most interesting physics occurs because of its incapability of tracking contact resonance accurately under rough topography. To overcome this difficulty, we develop high-throughput sequential excitation AFM that captures contact dynamics of probe-sample interaction with high fidelity and efficiency, acquiring the spectrum of data on each pixel over a range of frequencies that are excited in a sequential manner. Using electrochemically active granular ceria as an example, we map both linear and quadratic electrochemical strain accurately across grain boundaries with high spatial resolution where the conventional approach fails. The enhanced electrochemical responses point to the accumulation of small polarons in the space charge region at grain boundaries, thought to be responsible for the enhanced electronic conductivity in nanocrystalline ceria. The spectrum of data can be processed very efficiently by physics-informed principal component analysis (PCA), speeding data processing by orders of magnitude. The approach can be applied to a variety of AFM modes for studying a wide range of materials and structures at the nanoscale.

* Author to whom the correspondence should be addressed to: jjli@uw.edu.

INTRODUCTION

Atomic force microscopy (AFM) was invented in 1986,[1] and has since emerged as a powerful tool to probe a wide range of materials, structures, and systems with nanometer resolution.[2–6] Underlying the working principle of AFM is the dynamics of its cantilever, which is very sensitive to the sample-tip interactions, making it possible to probe a wide variety of functional properties.[7–13] Central to this operation is the resonance of the cantilever, tracking of which is essential to accurately capturing the material characteristics of interest, or substantial crosstalk and artifacts will be resulted.[14] This is particularly important for AFM operating in contact mode, such as piezoresponse force microscopy (PFM) [7,15–17] and electrochemical strain microscopy (ESM) [11,18–21], wherein contact resonance is greatly affected by not only material heterogeneity but also surface topography. For samples with rough surfaces, for example granular materials that are widely used in electrochemical conversion[21–23], accurate contact resonance tracking is rather challenging, and the spatial resolution is often compromised as a result.

A number of techniques have been developed to address this issue. For example, dual amplitude resonance tracking (DART) excites the cantilever using two frequencies across the resonance, and utilizes the difference in their amplitudes as the error signal for tracking.[24,25] This works reasonably well for smooth surface, but tracking often fails under rough topography.[13,14,26] Band excitation (BE) has also been developed by synthesizing a signal summing all harmonic excitation within a frequency band,[27] so that resonance is covered within the band and thus tracking becomes unnecessary. Nevertheless, the excitation power of BE is distributed among the band of frequencies, resulting in much reduced strength and signal-to-noise ratio (S/N) at each individual frequency.[27] Alternatively, a series of excitation signals of varying frequencies can be applied to the cantilever in sequential instead of concurrent manner, one frequency at a time, so that the signal strength and S/N are not compromised.[26] Such sequential excitation (SE) turns out to be very effective in capturing cantilever dynamics,[26] though it requires multiple scans that is not only slow and inefficient but also tend to induce drifting, probe wearing and surface damage that complicates the analysis. For sensitive electrochemical materials that are not very stable, such as halide perovskites,[28,29] we may not even have time to complete all the necessary scans.

Here we develop a high-throughput SE that is capable of accurately capturing cantilever dynamics, and thus underlying physical interactions, in just one instead of multiple scans. It has

scanning speed comparable to conventional DART, yet with much enhanced spatial resolution as well as quantitative accuracy, especially in the interface where steep steps locate. The approach can be applied to any AFM modes that rely on cantilever resonance for imaging, and we demonstrate it here using ESM to probe defect-induced Vegard strain near grain boundaries in polycrystalline ceria. These defects (small polarons) are thought to accumulate near grain boundaries, leading to enhanced electronic conductivity in nanoscrystalline ceria.[30,31] Using SE, we have mapped both the linear and quadratic electrochemical strains in ceria near grain boundaries at much higher resolution and fidelity than afforded by DART.

RESULTS

Failure of resonance tracking

Atomic force microscopy (AFM) works by probing its cantilever dynamics as affected by sample-tip interactions, which can be accurately described by damped harmonic oscillator model (DHO),[32]

$$A(\omega)=\frac{A_0\omega_0^2}{\sqrt{(\omega_0^2-\omega^2)^2+(\frac{\omega_0\omega}{Q})^2}},\qquad \phi(\omega)=\tan^{-1}[\frac{\omega_0\omega}{Q(\omega_0^2-\omega^2)}]+\phi_0, \quad (1)$$

where A_0, ϕ_0, Q, ω_0 are intrinsic amplitude, phase, quality factor and resonance frequency of the system, respectively, that are of interests to us, while $A(\omega)$ and $\phi(\omega)$ are measured amplitude and phase at excitation frequency ω. In order to track shifting resonance during scan, which is essential to accurately capture the sample-tip interactions, DART measures two pairs of amplitude and phase as $[A_1(\omega_1),\phi_1(\omega_1)]$ and $[A_2(\omega_2),\phi_2(\omega_2)]$ at two excitation frequencies ω_1 and ω_2, utilizing the difference between $A_1(\omega_1)$ and $A_2(\omega_2)$ as error signal for feedback control. One set of $A_1(\omega_1)$ mappings carefully acquired during trace and retrace scanning using DART on granular ceria overlaid on its 3D topography are shown in Fig. 1a, which covers one grain and a number of grain boundaries, with more data presented in Fig. S1 of Supporting Information (SI). The scale of colorbar is set for the best image contrast, so values on the colorbar of Fig. 1a do not mean the real range [1.3, 3.5]. While the trace and retract mappings resemble each other well in most part of the scans, closer examination reveals that they differ substantially at grain

boundaries. This is made clearer by the comparison of line scans shown in Fig. 1b, where it is evident that during trace the amplitude is reduced at the grain boundaries while under the retrace, it is enhanced. As such, the trends are completely opposite between trace and retrace at grain boundaries, while away from grain boundaries they agree with each other well. This difference highlights the failure of resonance tracking when there is significant topography variation often encountered in materials, even though the scan is carried out slowly with careful adjusted parameters to ensure the reliable tracking. For more casual scans, the problem will be more serious, as seen in Fig. 1c with more data in Fig. S2, where there are noticeable wavelet scratch-like patterns in the mapping of frequency ω_1 that extends along the scanning direction of the probe, especially at grain boundaries. Such artifact clearly indicates the failure of resonance tracking, even within a grain where topography variation is insignificant, and such mappings are not reliable even for qualitative analysis.

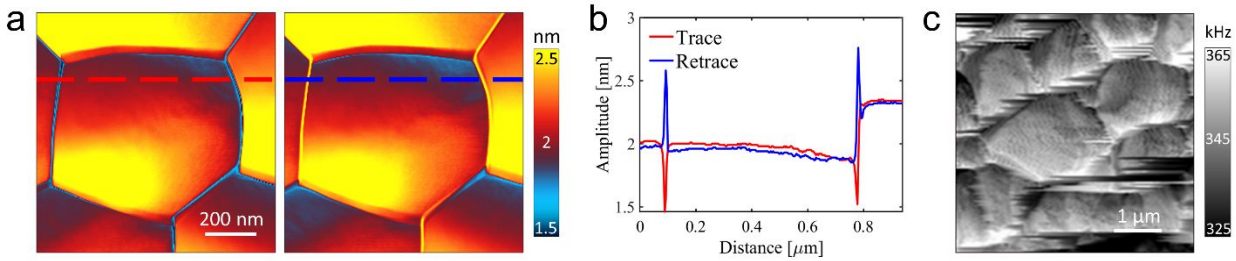

Fig. 1 The difficulty and failure of resonance tracking; (a) amplitude mappings from trace and retrace acquired under DART; (b) comparison of corresponding line scans between trace and retrace; (c) artifacts in the mapping of excitation frequency.

High-throughput sequential excitation

One solution to overcome the difficulties of resonance tracking is to eliminate it all together, for example by exciting the cantilever over a range of frequencies that cover the resonance. Band excitation (BE) implements this concept by applying all the frequencies concurrently,[27] while sequential excitation (SE) carries this out in a sequential manner.[26,33] The difference between these two approaches seems subtle, yet the implication is significant. The excitation power under SE is concentrated in each individual frequency, while for BE it is distributed over the entire band, and thus SE has much stronger signal strength and S/N. Original SE requires multiple

scans each with a distinct excitation frequency, which can be implemented on any standard AFM. Yet it is time consuming and prone to shifting during different scans, and it tends to induce probe wearing and sample damage. Here, we develop an advanced implementation for high-throughput SE that requires just one scan, as schematically shown in Fig. 2.

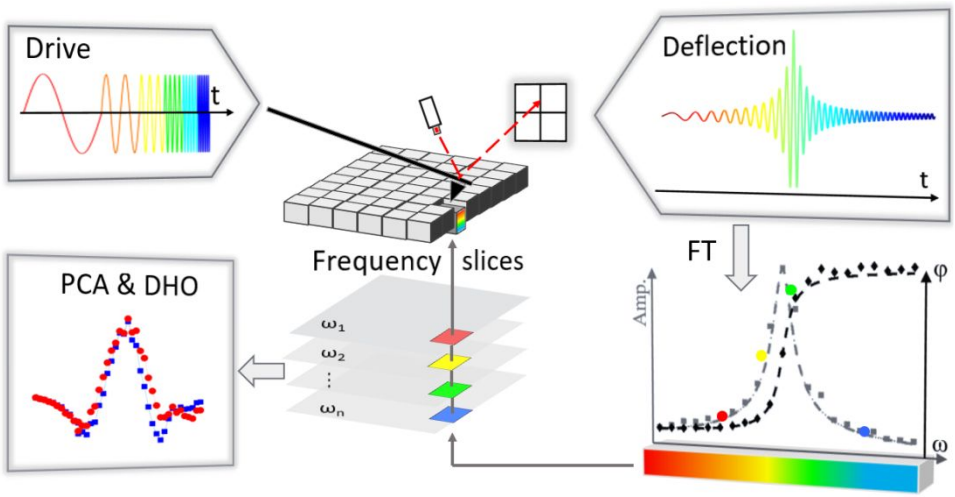

Fig. 2 Schematic of high-throughput SE-ESM.

Central to our approach is a high-resolution waveform designated as Drive in Fig. 2 drawn in time domain, where it is seen that the frequency increases over the time. This drive signal consists of *m* jointed sinusoidal waves with discrete frequencies, which can be produced by Arbitrary Waveform Generator (AWG) for each pixel during scan, as detailed in Fig. S3. The resulting deflection signal of cantilever at each pixel is recorded in time domain, and then Fourier transformed into frequency domain using the corresponding drive as a reference. This is equivalent to a digital lock-in, from which *m* pairs of amplitude and phase are obtained at each pixel over the frequency range of interest. As a demonstration, actual excitation and response in one of our experiments are presented in Fig. 3. The drive consists of 15 sinusoidal waveforms with distinct frequencies ranging from 347 to 390 kHz connected in sequential manner over a time span of 2.14 ms, as seen in Fig. 3a, with 3 such waveforms zoomed in in Fig. 3b. Each waveform lasts 50 cycles, leaving sufficient time to acquire response data accurately, corresponding to a line scan rate of 0.8 Hz that is comparable to a typical DART - it takes just 5 min to complete a 256×256 pixels scan. The response is recorded in time domain, as shown in Fig. 3cd, which contains large volume of data and is quite noisy. Yet after Fourier transformed

into frequency domain, a clear resonant peak emerges in amplitude, upon which phase jumps by 180°, as shown in Fig. 3ef along with drive signal. Such dynamics is expected from DHO governed by Eq. (1), and this illustrates how high-throughput SE works on signal generation as well as data acquisition and processing.

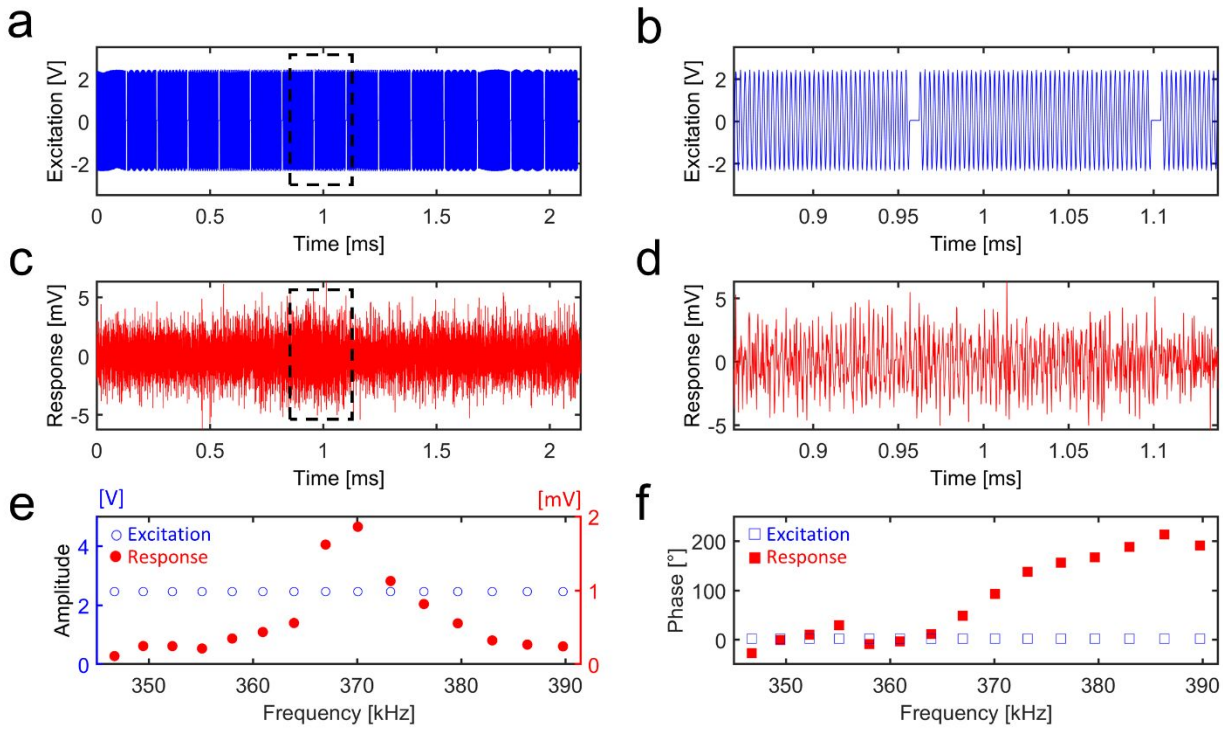

Fig. 3 Excitation and response of SE in time- and frequency-domains; (ab) drive in time domain; (cd) response in time domain; (ef) drive and response in frequency domain.

Linear and quadratic electrochemical strains

We now apply high throughput SE to probe linear and quadratic electrochemical strains of granular ceria via first and second harmonic ESM measurements,[34,35] for which high fidelity mappings at grain boundaries are essential to examine the proposed accumulation of space charges in its interfacial regions. Since a sequence of $A(\omega_i)$ and $\phi(\omega_i)$ are acquired under SE at each pixel, which can be fitted by Eq. (1) of DHO as shown by Fig. S4, we can obtain parameters intrinsic to the probed system, including intrinsic amplitude, phase, quality factor, and resonant frequency. Note that both amplitude and phase equations can be used, yielding consistent mappings as shown in Fig. S4.

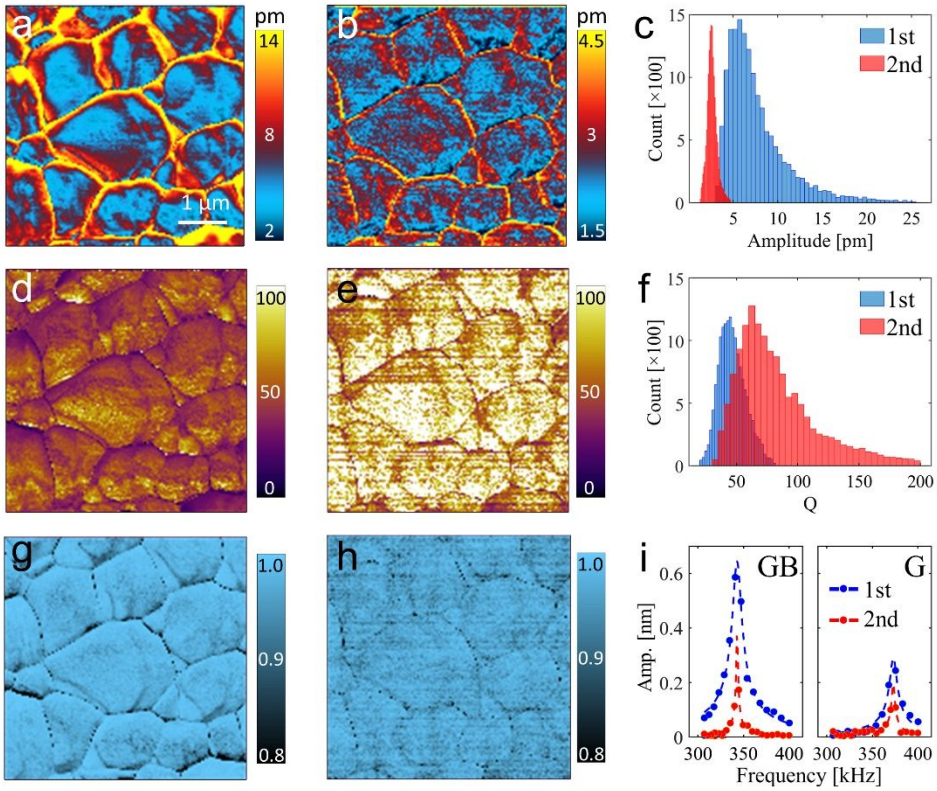

Fig. 4 Linear and quadratic strains in granular ceria; amplitude mappings of first (a) and second (b) harmonic responses, and their histogram distribution (c); quality factor mappings of first (d) and second harmonic measurement (e), and their histogram distribution (f); mappings of R^2 of first (g) and second (h) harmonic responses indicating DHO fitting fidelity; and (i) point-wise first and second harmonic response at grain boundaries and with a grain.

Linear electrochemical strain obtained as such is shown in Fig. 4a, acquired via first harmonic measurement at each of the excitation frequency, while quadratic strain is shown in Fig. 4b, acquired via second harmonic measurement at frequencies that doubles each excitation frequency. For both mappings, it is evident that the responses are substantially enhanced at the grain boundaries, which can be seen more clearly from point-wise comparison of first and second harmonic responses at grain boundaries and within a grain in Fig.4i. Furthermore, histogram distributions of first and second harmonic responses in Fig. 4c reveals that the electrochemical strain is predominantly linear, arising from Vegard strain due to fluctuations in small polaron concentration under the AC excitation, while the quadratic strain due to electrochemical dipole and thus electrostriction is also present.[35] Further insight can be learned

from the mappings of quality factors associated with first (Fig. 4d) and second (Fig. 4e) harmonic measurements, where it is observed that second harmonic electrostriction has higher quality factor (Fig. 4f), and thus smaller dissipation, as Vegard strain from small polarons is an energy-dissipative process. These observations are consistent with the proposed accumulation of space charges at grain boundaries, resulting in enhanced response at grain boundaries in both first and second harmonics.

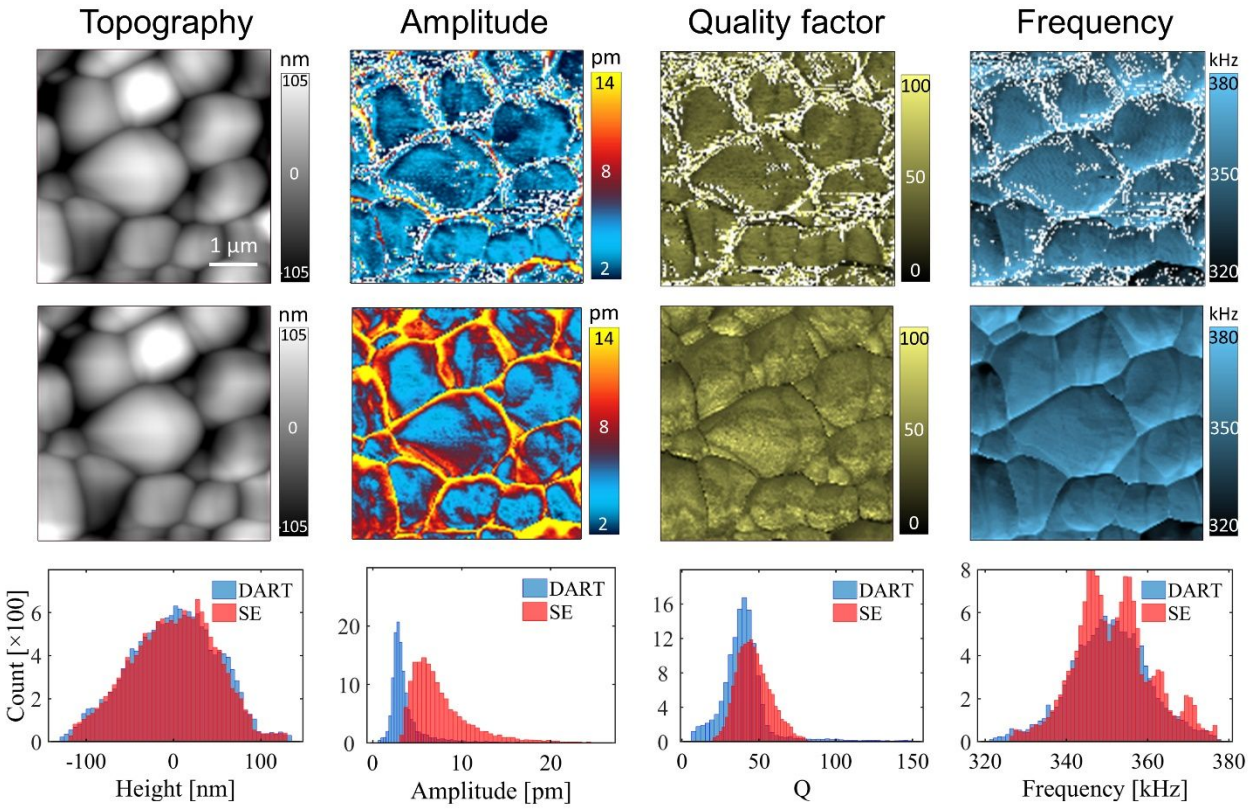

Fig. 5 Comparison of ESM mappings of ceria acquired by DART (first row) and SE (second row), along with their histogram distribution (third row).

We also examine the mappings of resonant frequencies from first and second harmonic measurements presented in Fig. S5, which match with each other well, demonstrating the high fidelity of the measurement. More importantly, we can examine the accuracy of the DHO fitting at each pixel in terms of R^2 coefficient,[36] a statistical measure on how close the data points are to the fitted regression line. Mappings of R^2 coefficients are presented in Fig. 4gh for first and

second harmonic measurements, ranging from 0.8 to 1.0 with respective mean values of 0.97 and 0.96, respectively, demonstrating high fidelity of the fitting. Even at grain boundaries, the fitting coefficients are mostly over 0.91. This is another advantage of SE, wherein the sequence of data enables us to accurately assess the reliability of DHO fitting for quantitative analysis. Under conventional DART, on the other hand, only two data points are available to solve the highly nonlinear DHO equations, which is not expected to be very accurate. Indeed, we compare the mappings of intrinsic amplitude, quality factor, and resonant frequencies acquired from DART and SE in Fig. 5, and it is evident that DART not only fails near the grain boundaries, as marked by all the white dots wherein there is no solution found for DHO, but it is also quantitatively different from SE, made evident by the comparison of histogram distributions in the amplitude – it underestimates the amplitude response substantially. Nevertheless, it is also quite remarkable to note that DART appears to be able to track the resonant frequency pretty well for the most part of grains, and majority of the issues occur at grain boundaries.

Data-accelerated physical analysis

While DHO is able to fit SE data accurately, it is a relatively slow process not amenable to real time control and adjustment, which is necessary for machine learning and artificial intelligence AFM that could be enabled by the big data generated under SE.[37] On the other hand, large volume of spectral information collected by SE is well suited for data analytics such as principal component analysis (PCA), which is highly efficient, though such pure statistical analytics often lacks a clearly physical insight. By carefully comparing underlying mathematics of both approaches, we are able to draw a close connection between PCA modes and DHO expansion,[26] rendering clear physical significance to otherwise purely statistical PCA modes. To this end, we first recast the 3D dataset of $\mathbf{A}(\omega, x, y)$ into a 2D matrix of $\mathbf{A}(\omega, n)$, where 2D spatial grid is collapsed into 1D. Here each row of $\mathbf{A}$ contains spatial data from a mapping scanned at a particular frequency, while each column represents spectral responses of a particular grid point acquired under various excitation. Principal component analysis (PCA) of $\mathbf{A}(\omega, n)$ can then be carried out through singular value decomposition (SVD),[38]

$$\mathbf{A} = \sum_{i=1}^{r} \sigma_i u_i w_i^T$$

where $\{u_i\}$ and $\{w_i\}$ are left and right singular vectors of **A**, corresponding to the principal spectral and spatial modes sorted by their singular values $\{\sigma_i\}$. In other words, any row/column of **A** can be represented with a combination of $\{u_i\}$ or $\{w_i\}$, separately.

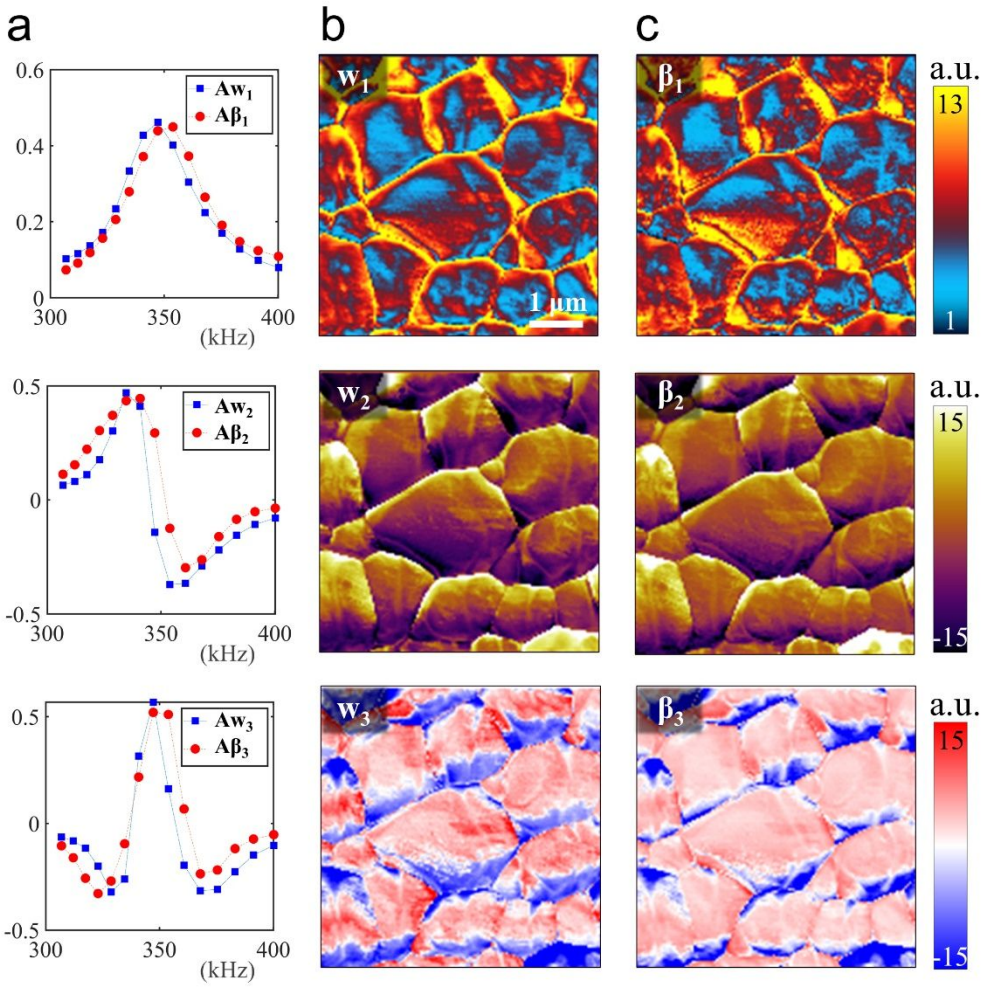

Fig. 6 Comparison of PCA modes and DHO expansion for first harmonic ESM data of granular ceria; (a) first three PCA spectral modes in comparison with corresponding DHO spectral basis; (b) first three PCA spatial modes; (c) corresponding DHO spatial basis.

In a parallel manner, we can also construct a new set of orthonormal modes from Taylor expansion series of DHO equation (1) via Gram–Schmidt process,[38] with $\boldsymbol{\beta}_1 = \mathbf{A}_0\mathbf{Q}\boldsymbol{\omega}_0$, and $\boldsymbol{\beta}_2$ and $\boldsymbol{\beta}_3$ derived from $\boldsymbol{\alpha}_2 = \mathbf{A}_0\mathbf{Q}\boldsymbol{\omega}_0 \circ (\boldsymbol{\omega}_0 - \bar{\boldsymbol{\omega}}_0)$ and $\boldsymbol{\alpha}_3 = \mathbf{A}_0\mathbf{Q}\boldsymbol{\omega}_0 \circ (\boldsymbol{\omega}_0 - \bar{\boldsymbol{\omega}}_0)^2$, where operator $\circ$ denotes the Hadamard product of two vectors, $\mathbf{A}_0\mathbf{Q}\boldsymbol{\omega}_0 = \mathbf{A}_0 \circ \mathbf{Q} \circ \boldsymbol{\omega}_0$, while overhead bar denotes

spatial averaging. It turns out that there is one-to-one correspondence between PCA modes and DHO expansion basis,[26] which is confirmed by the good agreement are shown in Fig. 6. The structural similarity (SSIM) (99.1%, 95.8%, and 94.3%) and Pearson correlation coefficients (PCC) (80.4%, 90.7%, and 83.9%) between PCA spatial modes and DHO basis in Fig. 6bc are pretty high, validating our analysis numerically. Note that PCA is much more efficient than DHO fitting, speeding up the data processing by 4 orders of magnitude, while we show that it provides essentially the same physical insight as DHO.

DISCUSSION

With ever-increasing hardware capabilities and computational powers, we are on the brink of a big data revolution for physical science [39–41] and AFM provides an ideal playground for the data-driven nanoscience that promises unprecedented new insight.[26,41–43] A good example is the recently developed G-mode AFM that relies on brute force big data analytics without pre-committing to a particular physical processes,[41,44] which is capable of uncovering "*unknown*" mechanisms underlying the physical systems. Here we adopt a more targeted approach, taking advantage of both physical understanding and data power. In particular, we design our excitation signals and data analysis specifically to capture cantilever resonance accurately, without acquiring too many redundant data, and ensuring that the data is clean and relevant to our physical system under the probe. As a result, our experimentation and analysis are highly efficient as well as accurate, which can be further accelerated by DHO-informed PCA analysis. Depending on particular systems under investigation, other forms of excitation signals can be designed and analyzed in a similar manner, for example by varying excitation amplitude for ferroelectric switching, and it is possible to implement a particular form of excitation on the demand. In a sense, our approach is well aligned with the movement from big data to deep data, *i.e.*, from data mining, correlation analysis, and unsupervised classification to causative data analytics that fuse physical understanding into big data.[2,40,45–48] For this purpose, innovative experimental and/or computational methodologies to acquire high quality (less noisy), efficient (less redundant), and physically relevant scientific data is essential, and this work is an attempt along this direction.

The power of our approach is best illustrated at the grain boundaries of ceria, wherein enhanced electrochemical strain is evident, attributed to their accumulation of space charges. Since SE does not depend on resonance tracking, it outperforms conventional approach as expected when it comes to large spatial variation. Moreover, SE is able to justify fitting results as well as the validity of raw data by taking advantages of multiple datapoints and statistics, while DART lacks this ability and is more vulnerable to various measurement errors with only two datapoints. As shown in Fig.5, even though maps probed by DART on grain looks relatively smooth, it may still underestimate response without awareness. Furthermore, we also conduct SE-ESM on a solid electrolytes $Li_{1.3}Al_{0.3}Ti_{1.7}(PO_4)_3$ at a high temperature (115℃), which is usually challenging for conventional resonance tracking due to continuous deformation of sample originating from environmental temperature variation. But the R^2 map of SE approach in Fig. S6e is overall greater than 0.9, implying it is still very trustworthy in a temperature-controlled environment, given that fitting is based on multiple datapoints. Therefore, we believe our high throughput SE will provide a powerful tool to resolve spatial variation of such cases with nanometer resolution.

CONCLUSIONS

In conclusion, we have developed a high-throughput AFM that captures electrochemical strain of ceria in just one scan, having scanning speed comparable to conventional DART, yet with much enhanced spatial resolution and high quantitative fidelity. This enables us to image accumulation of space charges across grain boundaries of ceria with nanometer resolution, and DHO-informed PCA has also been developed, speeding up the data analysis by orders of magnitude. The ideas can be applied to a variety of AFM modes for studying a wide range of materials and structures at the nanoscale, especially at the interfaces, and it embodies the spirit of deep data wherein targeted data acquisition and physics-informed data analytics prove to be powerful.

METHODS

DART-ESM

This measurement is performed on a Cypher AFM with an AC amplitude of 4 V applied to a Nanosensors PPP-EFM conductive probe. The scan rate is 1.0 Hz. the dynamics of the cantilever motion is characterized through built-in lock-in amplifiers, which physically reduces full time-domain information to limited frequency-domain data in terms of raw amplitudes and phases. The mappings of corrected amplitude, phase, resonant frequency, and quality factor were then calculated via DHO model.

SE-ESM

Both first and second harmonic resonance SE-ESM scanning were implemented using a UHF-AWG in combination with a Cypher AFM. Before scanning, the UHF-AWG has synthesized the desired waveform associated digital markers ready. Once the digital trigger from AFM is received, the AWG begins to convert the waveform into analog signals with 3.5 MHz ADC rate, which will then be fed into AFM to excite the probe. At the same time, a data acquisition (DAQ) system in UHF is also triggered and start to record the full motion of the probe in time domain via deflection channel of the AFM, sampling at 3.5 MHz. The synchronization is well tuned beforehand by adjusting the input waveform so that the excitation can work in parallel with the AFM XY scanners with delays less than 0.7 ms for each line, which is about a quarter of the scanning time for one pixel. The turn-around time between trace/retrace passes is enough for the DAQ to transfer the data to a computer for FT on-the-fly. The same sample and probe were used as DART-ESM measurement.

The design of SE waveform

The unit waveform used for one pixel usually consists of 15 different segments, each of which contains multiple periods of sinusoidal waves with a specific frequency belonging to [300 kHz, 400 kHz]. The amplitude of all sinusoidal waves is the same as DART-ESM used. Segment are sorted by the frequencies and jointed with 20 sampling points of zero amplitude, forming the unit waveform. Finally, the unit waveform is first jointed with 100 sampling points of zero amplitude, which helps the relaxation of the probe and the post-processing of data, and then repeated multiple times for one trace of scanning. Parameters may be slightly changed in real experiment

to meet the requirement of synchronization mentioned above. For the first harmonic measurement, the input waveform is also used as the reference wave of FT. For the second harmonic measurement, the input waveform is repeated once and then half sampled to generate the reference wave of FT, considering that the sample response was measured at double frequency of the excitation.

Principal components analysis

PCA is a statistical procedure that converts a set of observations of possibly correlated variables into a set of linearly uncorrelated variables called principal components. In this work, PCA is computed via SVD function in MATLAB, that is

$$\mathbf{A} = \mathbf{U}\mathbf{\Sigma}\mathbf{W}^T = \sum_{i=1}^{r} \sigma_i u_i w_i^T$$

where r is the rank of $\mathbf{A}$. Thus, spectral and spatial modes of dataset $\mathbf{A}$ corresponds to the left and right singular vectors ($\{u_i\}$ and $\{w_i\}$) of $\mathbf{A}$, which are ranked in the order of their importance (or say singular values $\{\sigma_i\}$). According to low rank approximation, $\mathbf{A}$ can be perfectly reconstructed by using first p modes if the last r-p+1 singular values are below the level of noise,

$$\mathbf{A} = \sum_{i=1}^{r} \sigma_i u_i w_i^T \approx \sum_{i=1}^{p} \sigma_i u_i w_i^T \ .$$

In this sense, PCA is an efficient algorithm for dimension reduction and data compression.

Structural similarity

SSIM is a perceptual metric that quantifies the similarity between two images. It is the average of the local SSIM value map:

$$\mathrm{SSIM}(x,y) = \frac{(2\mu_a\mu_b + \mathrm{c}_1)(2\sigma_{ab} + \mathrm{c}_2)}{(\mu_a^2 + \mu_b^2 + \mathrm{c}_1)(\sigma_a^2 + \sigma_b^2 + \mathrm{c}_2)},$$

where μ_a, μ_b, σ_a, σ_b, σ_{ab} are the average, variance, and covariance of 4×4 windows a and b that are centered in the pixel (x, y) of two images. c_1, c_2 are two constants to stabilize the division with weak denominator.

Pearson correlation coefficient

PCC can take range of values from +1 to -1. A value of 0 implies that there is no linear correlation between two vectors X and Y that are reshaped from two images respectively, while +1 means total positive linear correlation and −1 means total negative linear correlation.

$$P_{X,Y} = \frac{\sigma_{XY}}{\varsigma_X \varsigma_Y}$$

where σ_{XY} is the covariance and ς_X, ς_Y are the standard deviation of X and Y.

DATA AVAILABILITY

The data that support the findings of this study are available from the corresponding author upon request.

AUTHOR CONTRIBUTIONS

J.L. conceived and supervised the project. B.S. G. grew the ceria sample under the guidance of S.B. A. B.H. carried out AFM studies with the assistance of E. N.E and J.Y. J.L. wrote the manuscript and all authors participated in the revision and discussion.

ACKNOWLEDGMENTS

We acknowledge the support by US NSF through Materials Research Science and Engineering Center (DMR-1719797) SuperSeed Award and Chemical Measurement & Imaging Program (CHE-1708376). The instrumentation at SIAT was carried out with the support of NSFC of China (11627801) and Key Area R&D Program of Guangdong Province (2018B010109009)

ADDITIONAL INFORMATION

Competing interests: The Authors declare no Competing Financial or Non-Financial Interests.

REFERENCES

1 G. Binnig, C. F. Quate and C. Gerber, *Phys. Rev. Lett.*, 1986, **56**, 930.

2 S. V Kalinin, E. Strelcov, A. Belianinov, S. Somnath, R. K. Vasudevan, E. J. Lingerfelt, R. K. Archibald, C. Chen, R. Proksch, N. Laanait and S. Jesse, *ACS Nano*, 2016, **10**, 9068–9086.

3 S. V Kalinin and A. Gruverman, *Scanning probe microscopy: electrical and electromechanical phenomena at the nanoscale*, Springer Science & Business Media, 2007, vol. 1.

4 T. Li and K. Zeng, *Adv. Mater.*, 2018, **30**, 1803064.

5 B. Huang, G. Kong, E. N. Esfahani, S. Chen, Q. Li, J. Yu, N. Xu, Y. Zhang, S. Xie, H. Wen, P. Gao, J. Zhao and J. Li, *npj Quantum Mater.*, 2018, **3**, 30.

6 G. Zhong, F. An, Y. Bitla, J. Wang, X. Zhong, J. Yu, W. Gao, Y. Zhang, C. Tan and Y. Ou, *ACS Nano*, 2018, **12**, 9558–9567.

7 A. Gruverman and S. V Kalinin, *J. Mater. Sci.*, 2006, **41**, 107–116.

8 A. Majumdar, *Annu. Rev. Mater. Sci.*, 1999, **29**, 505–585.

9 T. W. Kelley, E. Granstrom and C. D. Frisbie, *Adv. Mater.*, 1999, **11**, 261–264.

10 J. Li, J.-F. Li, Q. Yu, Q. N. Chen and S. Xie, *J. Mater.*, 2015, **1**, 3–21.

11 A. N. Morozovska, E. A. Eliseev, N. Balke and S. V Kalinin, *J. Appl. Phys.*, 2010, **108**, 53712.

12 S. Li, Y. Zhou, Y. Zi, G. Zhang and Z. L. Wang, *ACS Nano*, 2016, **10**, 2528–2535.

13 E. N. Esfahani, T. Li, B. Huang, X. Xu and J. Li, *Nano Energy*, 2018, **52**, 117–122.

14 S. Bradler, A. Schirmeisen and B. Roling, *J. Appl. Phys.*, 2018, **123**, 035106.

15 D. A. Bonnell, S. V. Kalinin, A. L. Kholkin and A. Gruverman, *MRS Bull.*, 2009, **34**, 648–657.

16 R. K. Vasudevan, N. Balke, P. Maksymovych, S. Jesse and S. V. Kalinin, *Appl. Phys. Rev.*,

2017, **4**, 021302.

17 Y. Liu, H.-L. Cai, M. Zelisko, Y. Wang, J. Sun, F. Yan, F. Ma, P. Wang, Q. N. Chen and H. Zheng, *Proc. Natl. Acad. Sci.*, 2014, **111**, E2780–E2786.

18 J. Zhu, L. Lu and K. Zeng, *ACS Nano*, 2013, **7**, 1666–1675.

19 N. Balke, S. Jesse, A. N. Morozovska, E. Eliseev, D. W. Chung, Y. Kim, L. Adamczyk, R. E. García, N. Dudney and S. V Kalinin, *Nat. Nanotechnol.*, 2010, **5**, 749.

20 R. Giridharagopal, L. Q. Flagg, J. S. Harrison, M. E. Ziffer, J. Onorato, C. K. Luscombe and D. S. Ginger, *Nat. Mater.*, 2017, **16**, 1–6.

21 S. Duan, H. Jin, J. Yu, E. N. Esfahani, B. Yang, J. Liu, Y. Ren, Y. Chen, L. Lu and X. Tian, *Nano Energy*, 2018, **51**, 19–25.

22 D. O. Alikin, K. N. Romanyuk, B. N. Slautin, D. Rosato, V. Y. Shur and A. L. Kholkin, *Nanoscale*, 2018, **10**, 2503–2511.

23 Q. Nataly Chen, Y. Liu, Y. Liu, S. Xie, G. Cao and J. Li, *Appl. Phys. Lett.*, 2012, **101**, 63901.

24 B. J. Rodriguez, C. Callahan, S. V Kalinin and R. Proksch, *Nanotechnology*, 2007, **18**, 475504.

25 A. Gannepalli, D. G. Yablon, A. H. Tsou and R. Proksch, *Nanotechnology*, 2011, **22**, 355705.

26 B. Huang, E. N. Esfahani and J. Li, *Natl. Sci. Rev.*, 2018, **6**, 55–63.

27 S. J. and S. V. K. and R. P. and A. P. B. and B. J. Rodriguez, *Nanotechnology*, 2007, **18**, 435503.

28 S. Chen, X. Zhang, J. Zhao, Y. Zhang, G. Kong, Q. Li, N. Li, Y. Yu, N. Xu and J. Zhang, *Nat. Commun.*, 2018, **9**, 4807.

29 R. Wang, M. Mujahid, Y. Duan, Z.-K. Wang, J. Xue and Y. Yang, *Adv. Funct. Mater.*, 2019, **0**, 1808843.

30 Q. N. Chen, S. B. Adler and J. Li, *Appl. Phys. Lett.*, 2014, **105**, 1–5.

31 S. Kim and J. Maier, *J. Electrochem. Soc.*, 2002, **149**, J73–J83.

32 A. P. French, *Vibrations and waves*, CRC press, 1971.

33 P. Jiang, B. Huang, L. Wei, F. Yan, X. Huang, Y. Li, S. Xie, K. Pan, Y. Liu and J. Li, *Nanotechnology*, 2019, **30**, 205703.

34 Q. Nataly Chen, Y. Ou, F. Ma, J. Li, Q. N. Chen, Y. Ou, F. Ma, J. Li, Q. N. Chen, Y. Ou, F. Ma and J. Li, *Appl. Phys. Lett.*, 2014, **242907**, 1–5.

35 J. Yu, E. N. Esfahani, Q. Zhu, D. Shan, T. Jia, S. Xie and J. Li, *J. Appl. Phys.*, 2018, **123**, 155104.

36 S. A. Glantz and B. K. Slinker, *Primer of Applied Regression and Analysis of Variance*, 1990.

37 B. Huang, Z. Li and J. Li, *Nanoscale*, 2018, **10**, 21320–21326.

38 W. H. Greub, *Linear algebra*, Springer Science & Business Media, 2012, vol. 23.

39 J. Hill, G. Mulholland, K. Persson, R. Seshadri, C. Wolverton and B. Meredig, *MRS Bull.*, 2016, **41**, 399–409.

40 J. Byers, *Nat. Phys.*, 2017, **13**, 718.

41 A. Belianinov, S. V. Kalinin and S. Jesse, *Nat. Commun.*, 2015, **6**, 6550.

42 H. Trivedi, V. V. Shvartsman, M. S. A. Medeiros, R. C. Pullar and D. C. Lupascu, *npj Comput. Mater.*, 2018, **4**, 1–7.

43 R. Giridharagopal, J. T. Precht, S. Jariwala, L. Collins, S. Jesse, S. V. Kalinin and D. S. Ginger, *ACS Nano*, 2019, **13**, 2812–2821.

44 L. Collins, M. Ahmadi, T. Wu, B. Hu, S. V Kalinin and S. Jesse, *ACS Nano*, 2017, **11**, 8717–8729.

45 S. Munevar, *Nat. Biotechnol.*, 2017, **35**, 684.

46 Y. Ruihao, L. Zhen, B. P. V., X. Deqing, Z. Yumei, D. Xiangdong, S. Jun, X. Dezhen and L. Turab, *Adv. Mater.*, 2018, **30**, 1702884.

47 D. S. Kermany, M. Goldbaum, W. Cai, C. C. S. Valentim, H. Liang, S. L. Baxter, A. McKeown, G. Yang, X. Wu, F. Yan, J. Dong, M. K. Prasadha, J. Pei, M. Ting, J. Zhu, C. Li, S. Hewett, J. Dong, I. Ziyar, A. Shi, R. Zhang, L. Zheng, R. Hou, W. Shi, X. Fu, Y. Duan, V. A. N. Huu, C. Wen, E. D. Zhang, C. L. Zhang, O. Li, X. Wang, M. A. Singer, X. Sun, J. Xu, A. Tafreshi, M. A. Lewis, H. Xia and K. Zhang, *Cell*, 2018, **172**, 1122-1131.e9.

48 Y. Liu, T. Zhao, W. Ju and S. Shi, *J. Mater.*, 2017, **3**, 159–177.

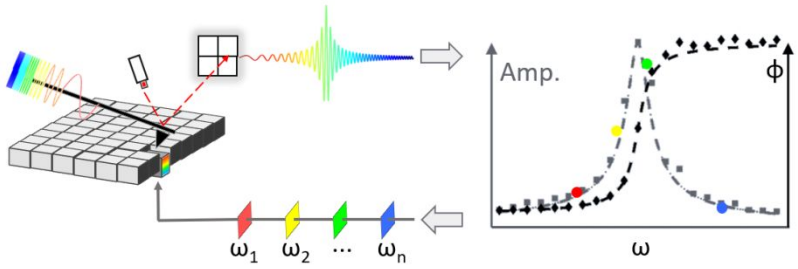

A high-throughput AFM integrating efficient sequential excitation, targeted data acquisition and physics-informed data analytics.